MODELLING AND ASSESSMENT OF THE CURRENT AND FUTURE SPACE SURVEILLANCE NETWORK

J. Geul, E. Mooij, and R. Noomen

Astrodynamics and Space Missions, Delft University of Technology, Kluyverweg 1, 2629 HS Delft, The Netherlands, Email: {j.geul, e.mooij, r.noomen}@tudelft.nl

ABSTRACT

Two-Line Elements (TLEs) and Tracking and Impact Predictions (TIPs) resulting from the Space Surveillance Network (SSN) are important for many Space Situational Awareness (SSA) activities. The network consists of many different radar and optical stations, contributing in either a dedicated, collateral or contributing fashion. For the majority of objects in low-Earth orbit (LEO) phased-array radar (PAR) stations are essential for maintaining the satellite catalog (SATCAT). A survey of the current state of the SSN and a methodology for simulating the network is presented. The current state is compared to a future scenario with the new Space Fence System (SFS) included. The SSN is simulated as a collection of current and hypothetical dedicated and collateral PARs. The location and coverage of each sensor is investigated and modelled. Observations are generated for a test rocket body in LEO. TLEs are estimated from the simulated measurements using the Simplified General Perturbations (SGP4) model. The sensitivity of the fit residuals and propagated accuracy with respect to eccentricity, inclination, and number of observations and sensors is analysed. The orbit-determination solution is found to be most sensitive to the eccentricity, and number of observations and sensors involved. The new SFS improves the solution, especially for lower inclinations.

Key words: Space Debris; Space Surveillance; Phased-Array Radar; Satellite Catalog (SATCAT); Orbit Determination; Two-Line Elements (TLEs).

1. INTRODUCTION

The Space Surveillance Network (SSN) is responsible for tracking over 18 000 objects in the satellite catalog (SATCAT) [1]. Its measurements are used for generating Two-Line Elements (TLEs) and Tracking and Impact Predictions (TIPs). These products are often the only available source for many Space Situational Awareness (SSA) activities, such as conjunction analyses and re-entry predictions. The SSN is the largest network of its kind and consists of optical and radar sensors. The sensors contribute in various degrees, and are classified as either dedicated, collateral or contributing. Most sensors are located on the north-western hemisphere. The new Space Fence System (SFS), with two sites in the Pacific Ocean and Australia, promises improved network geometry and detection capabilities.

To properly assess the current and future configurations of the SSN, the technical capabilities, coverage, roles, and location of individual sensors must be taken into account. Previous surveys of the SSN are a good starting point, but are either lack completeness in these aspects or are outdated [1, 2, 3, 4, 5].

This paper presents a survey of the most important sensors, focusing on sensor type, role, coverage, and capabilities. The current network geometry is simulated. A methodology for generating and editing observations will be presented.

For this study the tracking of rocket bodies in low-Earth orbit (LEO) is considered. The focus is on phased-array radars (PARs), as they are primarily used for this purpose. TLEs are estimated from these simulated observations for a test rocket body. The sensitivity of the solutions to several orbital and orbit determination (OD) parameters is investigated. Finally, through the addition of two new sensors, the future network geometry is assessed.

The paper is outlined as follows. First, the SSN is described in Sec. 2. Section 3 presents an overview of the simulation set-up. The results are presented and discussed in Sec. 4. Finally, conclusions and recommendations are given in Sec. 5.

2. SPACE SURVEILLANCE NETWORK

The United States Air Force Space Command Space Surveillance Network (US AFSPC SSN) is the largest governmental network. The network was initially developed as a missile-warning network [4]. The network consists of plain radar, optical, and PAR sensors, and can be

[1] `https://www.celestrak.com/satcat/boxscore.asp`, retrieved: April 3, 2017

Table 1. Overview of PARs sensors in the SSN. The sensor role (R) is either dedicated (D) or collateral (C). The azimuth and elevation of the boresight of the radar face is indicated in degrees.

Name / location	Model	R	Lat [°]	Lon [°]	Alt [m]	Boresight [°]
Eglin, FL, US	AN/FPS-85	D	30.572	−86.215	36	180x45
Clear[a], AK, US	AN/FPS-132	C	64.300	−149.191	175	6,244x20
Fylingdales, UK	AN/FPS-132	C	54.362	−0.670	258	5,125,245x20
Thule, GL	AN/FPS-132	C	76.569	−68.299	424	117,357x20
Beale, CA, US	AN/FPS-132	C	39.136	−121.351	117	186,246x20
Cape Cod[a], MA, US	AN/FPS-132	C	41.752	−70.538	67	47,167x20
Cobra Dane, Shemya, AK, US	AN/FPS-108	C	52.737	174.092	68	319x20
PARCS, Cavalier ND, US	AN/FPQ-16	C	48.725	−97.900	344	8x25
SFS1[b], Kwajalein Atol, US	AN/FSY-3	D	8.723	167.719	7	0x90
SFS2[b], Exmouth, AU	AN/FSY-3	D	−21.816	114.165	11	0x90

[a] The upgrades of the Clear and Cape Cod started in 2012 and 2013 and are to be fully certified in 2017 and 2018, respectively [6].

[b] SFS1 will become operation in 2018, while SFS2 is expected to become operational in 2021 [7].

grouped into dedicated, collateral, and contributing sensors. Dedicated sensors have space surveillance as a primary mission. Collateral sensors are connected directly to the Space Surveillance Center (SSC). These sensors still have primary (or even secondary) missions other than space surveillance. In the case of PARs, usually a dedicated sub-array of elements (also fence) is operated for the detection and tracking of objects. This fence covers only a portion of the total coverage and duty cycle, in parallel to the primary mission. Finally, contributing sensors provide space surveillance only upon request from the Joint Space Operations Center (JSpOC). The following examples give a rough idea of how much these sensors contribute [3]: the Millstone rader contributes 80 hours per week and the Haystack radar about one week every six. All four mechanical radars at Kwajalein contributed a total of 138 hours in 2014. Some sensors are only used exclusively for certain purposes, such as to track launches.

The two radar types currently used in the SSN are mechanical and PARs. Previously, the SSN also included a multi-static radar system (more details below). PARs consist of flat faces containing several thousands of antenna elements. Compared to mechanical radars, PARs use electronic steering by shifting the phase of incoming signals. Due to this, PARs can track numerous targets simultaneously and are suitable for detection [3]. PARs have a limited coverage (if less then three faces are used), narrowing beamwidth away from the face normal, lower operating frequencies, and higher cost.

In the past Several authors have consolidated space-surveillance sensors [1, 3, 4, 5]. Although they provide valuable information, none prove to be a complete and sufficient source for simulating the SSN. The SSN is rapidly changing, so even information a few years old can already be outdated. For example, the Air Force Space Surveillance System (AFSSS) and the Moron Optical Space Surveillance (MOSS) telescope were both closed in 2013, the Antigua radar was relocated to Australia in 2015, and the Ascension radar has become a dedicated sensor. Moreover, a categorisation into dedicated, collateral, and contributing sensors is important. Sensor limitations, such as coverage and range, have a large impact on the simulated observations. Lastly, instrument accuracy, observation rate, tasking, and scheduling should ideally all be taken into account.

The AFSSS formed a major asset for the radar surveillance for LEO satellites. Also known as the space fence, the AFSSS consisted of three continuous transmitter and six receiver stations at 33° latitude, spanning approximately 70° in longitude across the US. The fence was closed in August 2013. Construction of the AN/FSY-3 Space Fence System (SFS) began in 2014. SFS will consist of two sites and use S-band radar (2 GHz to 4 GHz). Traditional PARs operate at around 400 MHz, with the exception of Cobra Dane which has a nominal frequency of 1275 MHz [8]. The first and largest site is located on Kwajalein Atoll in the Pacific Ocean and is expected to be operational in 2018. The second and smaller site is located in Western Australia and is expected to be operational in 2021 [7]. The new fence will have a higher accuracy and detection capabilities than current sensors, potentially increasing the number of tracked objects to more than 100 000 [9].

An updated inventory of all SSN sensors is made, including all mechanical radars and optical stations. The closing, relocation, and upgrades of sensors are taken into account. The current role of each sensor is investigated, as well as a preliminary investigation into sensor accuracy. Tab. 1 shows a selection of this survey for PARs.

The table reports the azimuth and elevation of the normal of the radar faces (i.e., boresight). The horizontal field of view (FOV) is generally reported to be 120° (thus

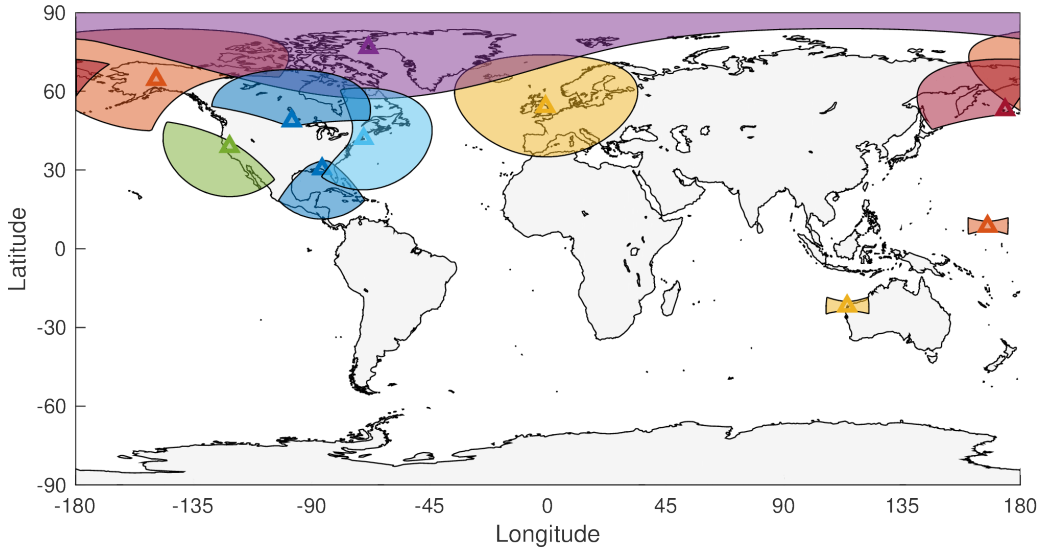

Figure 1. Space Surveillance network coverage for an object in a circular 600 km *orbit.*

a full 360° for three faces). For faces with a tilt of 20°, the resulting maximum elevation differs amongst sources, most report either 80° or 85° of maximum elevation. The latter value suggests a vertical FOV of 130°. However, it is assumed that the FOV of all PAR systems is 120° in horizontal and vertical direction per face, as they are roughly square. An exception is SFS, which receiving antenna array is more rectangular and spread in longitudinal direction, for this sensor a FOV of 40° is assumed for the latitudinal direction. The location of SFS1 was estimated from satellite images of the construction site. The location of SFS2 is unknown, but is assumed to be at the Naval Communication Station Harold E. Holt in Exmouth, Western Australia, although this is not confirmed.

The contract for the construction of a new AN/FPS-132 early-warning radar in Qatar was awarded to Raytheon and is expected to be completed in 2021 [10]. Its exact location, number of faces, and possible role in the SSN is not known.

3. SIMULATION SET-UP

The SSN is simulated for LEO. First, the configuration of the network is explained. Second, the test object is introduced, including a sampling strategy to randomise the orbits. Third, the set up of the orbit propagator is given. Fourth, the process of simulating observations is detailed. Finally, the orbit determination is explained.

3.1. Network Configuration

The coverage is dependent on the orbit of an object. Due to the FOV, the coverage grows with the range, resulting in longer observation arcs. A coverage map is generated for a test object in a 600 km orbit. The azimuth, elevation, and range is calculated of the test object with respect to each station using the WGS84 reference ellipsoid [2] and coordinates from Tab. 1. The observation vectors are then transformed to the local observation plane, as determined by the boresight of each face. Only observations within the FOV are kept.

Fig. 1 shows the location and coverage of the dedicated and collateral PARs for a test object in a circular orbit of 600 km. The elevation and azimuth limitations of each sensor have been taken into account. Single-, double-, and triple-face PARs are easily distinguished. The primary mission of many of these sensors is providing ballistic missile warnings, which is obvious from the outward facing coverage of the stations along the US border. The footprint of the two SFS sensors seems small in comparison to the other sensors. This is due to projecting the (mostly) vertical coverage on the horizontal plane, reduced latitudinal coverage, and choice of map projection (i.e., a tendency to exaggerate sizes at higher latitudes).

The figure also shows how most PARs are located in North America and northern Europe. In this configuration, the southern and eastern hemisphere are underrepresented. The two SFS sensors will improve geographic coverage.

3.2. Test Object

The Delta-K rocket body is selected as the test object. The object has frequently re-entered and fragments have been previously recovered due to its high-temperature resistant components. The Delta-K was also subject for the 6 degree-of-freedom (6DOF) re-entry simulator in [11].

[2] `http://earth-info.nga.mil/GandG/wgs84/index.html`, accessed: April, 7, 2017

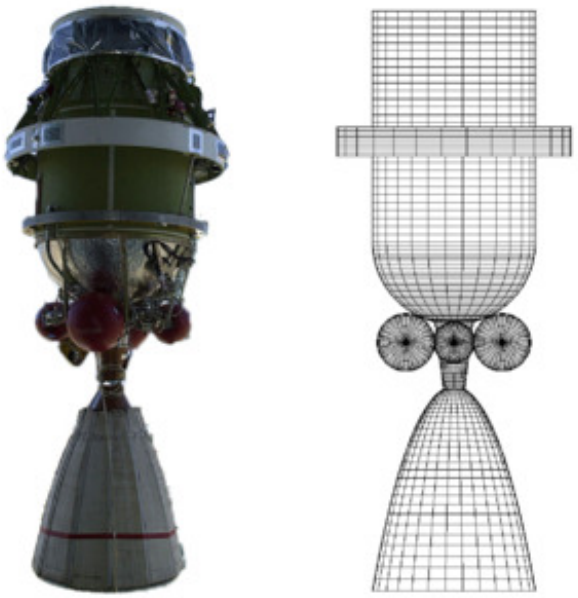

Figure 2. True and modelled Delta-K rocket body [11].

As the aerodynamic model and databases for the Delta-K were already derived, a 6DOF propagation of the test object is performed. Fig. 2 shows the true and modelled Delta-K rocket body.

A nominal state has been derived from 33 re-entered Delta-Ks in the period of 2004 to 2017. For each object the orbital state 30 days prior to re-entry is taken. The variations in semi-major axis, eccentricity, and inclination are shown in Fig. 3. A strong correlation between semi-major axis and eccentricity can be observed, related to the circularisation of the orbit due to the aerodynamic drag. Moreover, the objects have either a low or high inclination, depending on the target orbits in which these rockets were launched (i.e., GTO or LEO, respectively). The groups are indicated by the different markers, where the legend indicates the mean and standard deviation of the inclinations found in each group.

Random initial states are sampled from each group with an equal ratio. The eccentricity is sampled uniformly within the observed bounds. The semi-major axis is obtained through a linear correlation with the eccentricity. Finally, the inclination is sampled from a normal distribution. The right-ascension of the ascending node and argument of perigee are assumed to be uniformly distributed between 0 and 360°, and the initial true anomaly is zero. The initial aerodynamic angles are assumed to be zero, while the rotational rate is taken as one revolution per minute about the pitch axis. Finally, variations in the atmospheric density are modelled using a log-normal distribution with parameters $\mu^\star = 1.0$ and $\sigma^\star = 0.12$ [11].

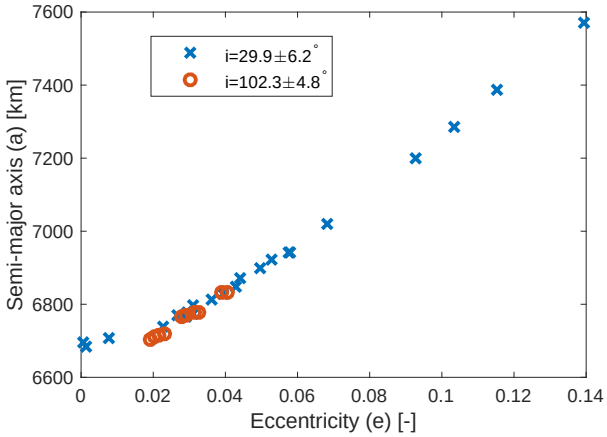

Figure 3. Semi-major axis versus eccentricity grouped by inclination of 33 Delta-K rocket bodies.

3.3. Orbit propagation

Observations are generated from numerically propagated orbits for the varying initial conditions. As mentioned previously, both the translational state and rotational state of the object is propagated. The equations of motion are integrated using a Runge-Kutta-Fehlberg 4(5) variable step-size integrator. The tolerance is set to $\epsilon_{rel} = \epsilon_{abs} = 1 \times 10^{-8}$. The step-size is allowed to vary between a minimum and maximum value of 1×10^{-4} and 1×10^{3} s, respectively. The EGM2008 gravity field model is used [3]. The atmospheric density is modelled using the NRLMSISE-00 model [12]. These settings provided a good trade-off between accuracy and computational efficiency.

3.4. Observations

Realistically, observations are limited by a number of technical and physical constraints, and are subject to numerous error sources. Not properly taking these into account would lead to too many and too idealistic observations. Accurate modelling of individual sensor capabilities, and scheduling is difficult based on the available information, and therefore considered beyond the scope of the current work. The main focus is on modelling the network geometry and coverage.

The observation conditions are taken into account for each sensor, as previously explained in Sec. 3.1. An elevation cut-off of 5° is used for all sensors. A measurement rate of 0.1 Hz has been chosen. The measurements are further edited to account for sensor availability, viewing conditions, and other limitations. The process uses an observation probability factor to discard measurements. An individual observation has a 20% chance of being re-

[3] `http://earth-info.nga.mil/GandG/wgs84/gravitymod/egm2008/egm08_wgs84.html`, retrieved: April 7, 2017.

jected, while the probability for discarding an entire pass is 25% for collateral sensors only.

Measurement noise is simulated to account for sensor capabilities and atmospheric disturbances. The noise is assumed to be unbiased Gaussian noise, with a standard deviation of $1\,\mathrm{km}$ in radial direction and 0.1° ($1\,\mathrm{km}$ at $r = 600\,\mathrm{km}$) in azimuth and elevation.

3.5. Orbit Determination

The observations are used to fit TLEs using the Simplified General Perturbations (SGP4) model [13]. Range, azimuth and elevation measurements are generated for each MC sample for three consecutive days. The fit span consists of the first two days of observations. These are in the form of range, azimuth, and elevation, which are edited and used to for orbit fitting. The test span consists of the third and final day and provides unedited observations in inertial Cartesian coordinates, which are used for studying the propagation accuracy of the solution.

4. RESULTS

The orbit determination is performed for 1000 randomly initialised orbits. The mean, median, and standard deviation of the fit and test span are collected for each sample.

On average, the object is observed by 4.8 stations over two days, resulting in 1560 observations. The mean fit residual is $1.7\,\mathrm{km}$, while the residuals for test period are on average $5.8\,\mathrm{km}$. The large error growth in the test period is due to the low orbit and resulting atmospheric drag, and in line with actual results for one-day predictions of TLEs [14].

4.1. Sensitivity

The rank correlation between the median residual and a number of parameters is computed to obtain the sensitivity of the solution. Fig. 4 shows the result for the fit and test span for 5 parameters: eccentricity, inclination, density, number of stations, and number of observations, respectively. The results between the fit and test span are very similar. The correlations are slightly larger for the test span, which are enhanced through propagation and the resulting error growth.

The residuals are negatively correlated with the eccentricity and number of observations. Near-circular orbits are more difficult to estimate due to sensitivity of the argument of perigee near its singularity. The reduction of the residuals with the number of observations is obvious. However, there is a strong positive correlation with the number of stations. It is found that the spread of solutions increases significantly with multiple stations. Some

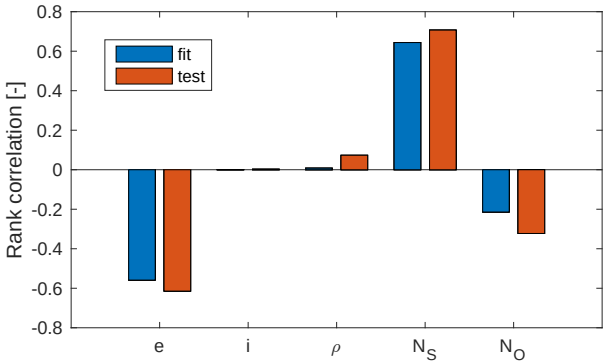

Figure 4. Sensitivity of orbit fit and propagation to the eccentricity e, inclination i, density ρ, number of stations N_s, and number of observations N_o.

solutions are improved, while other are worsened. Improved performance can be achieved by only including observations from sensors, if the fit is improved.

Inside each inclination group the variation has little effect the solution quality. However, there is a small difference between the two groups, which will be discussed next.

4.2. Space Fence

Fig. 5 shows the residuals of the test span for the two inclination groups (L and H, indicating the lower and higher inclinations, respectively) and two observation scenarios (C and F indicating the current and future scenarios, respectively).

It can be seen that the lower-inclined group has a slightly higher accuracy, but larger spread. The difference is attributed to the larger spread in eccentricity for the lower-inclined group. The additional sensors have a positive effect on the orbit solutions. The mean of the lower-inclined objects is reduced with $650\,\mathrm{m}$, while the higher-inclined mean is reduced by $257\,\mathrm{m}$. The larger difference for the low-inclined group is due to the location of the new sensors closer to the equator.

More detailed modelling of these sensors will likely improve these results further, as the SFS is expected to be more accurate that other PARs [7]. The spread of the solutions is higher, especially for the higher-inclined objects, which is due to the small number of observations resulting from short passes registered by the SFS sensors. The passes are shorter then for traditional PARs due to the vertical boresight and narrow latitudinal width of the fence. For a near-polar orbit the pass duration is only several minutes.

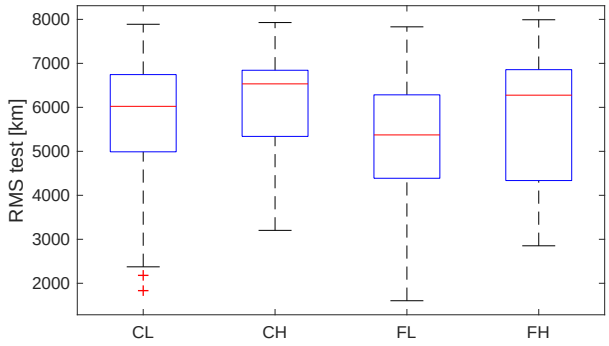

Figure 5. Boxplot of the propagated residuals for one day for the current and future network configuration (C and F, respectively) and the low- and high-inclined orbits (L and H, respectively).

5. CONCLUSIONS

The SSN is continuously changing. New sensors are added, as existing ones are relocated, upgraded, or closed. Moreover, the participation of sensors can change over time. An overview of the current configuration was presented for PARs, including the planned SFS. The coverage of each sensor was investigated. Observations for a Delta-K rocket-body reference object were generated for a randomly initialised orbit with varying eccentricity, inclination, and atmospheric density. From the observations the TLEs were estimated.

The residuals of both the fit and test span are highly sensitive to the eccentricity, number of observations, and number of sensors, while the inclination has minor influence.

The two additional SFS sensors provide a reduction of the median error in the solutions, especially for low-inclined orbit. However, due to the shorter observation arcs, the spread in solution quality is increased.

The study only took the network geometry into account. Further improvements can be made by simulating the accuracy of individual sensors to a higher degree. The capabilities are found to differ greatly across sensors. Specifically, the SFS promise a significant improvement in performance over traditional PARs. So the observed benefits are likely very conservative and much higher in reality. However, more details on the sensors are required, and these are often not available.

ACKNOWLEDGEMENT

This work is supported by the European Office for Aerospace Research and Development (EOARD), grant FA9550-14-1-0344.

REFERENCES

1. Johnson, N. L., "U.S. Space Surveillance," *Advances in Space Research*, Vol. 13, No. 8, 1993, pp. 5–20.
2. Klinkrad, H., Fritsche, B., and Koppenwallner, G., "Re-Entry Prediction and On-Ground Risk Estimation," *Space Debris - Models and Risk Analysis*, edited by H. Klinkrad, chap. 9, Springer Verlag, Berlin.
3. Chatters, E. and Crothers, B. J., "Space Surveillance Network," *Space Primer AU-18*, Vol. 18, 2nd ed., 2009, pp. 249–258.
4. Vallado, D. A. and Griesbach, J. D., "Simulating Space Surveillance Networks," *AAS/AIAA Astrodynamic Specialist Conference*, 2011.
5. Flohrer, T., *Optical Survey Strategies and their Application to Space Surveillance*, Schweizerischen Geodätischen Kommission, Zurich, 2012.
6. Missile Defense Agency, "Upgraded Early Warning Radars, AN/FPS-132," Tech. Rep. Fact Sheet 16-MDA-8777, 2016.
7. Hack, P. J., Carbaugh, K., and Simon, K. J., "Automated Space Surveillance Using the AN/FSY-3 Space Fence System," *Advanced Maui Optical and Space Surveillance Technologies*, 2016.
8. Allen, R. S., Donatelli, D. E., and Picardi, M. C., "Correction for Ionospheric Refraction for COBRA DANE," *Air Force Surveys in Geophysics*, , No. 376, 1977.
9. Pechkis, D. L., Pacheco, N. S., and Botting, T. W., "Statistical Approach to the Operational Testing of Space Fence," *IEEE Aerospace and Electronic Systems Magazine*, Vol. 31, No. 11, 2016, pp. 30–39.
10. Binnie, J., "Qatari long-range radar procurement moves forward," *IHS Jane's Defence Weekly*, dec 2016.
11. Ronse, A. and Mooij, E., "Statistical Impact Prediction of Decaying Objects," *Journal of Spacecraft and Rockets*, Vol. 51, No. 6, 2014, pp. 1797–1810.
12. Picone, J. M., Hedin, A. E., Drob, D. P., and Aikin, A. C., "NRLMSISE-00 Empirical Model of the Atmosphere: Statistical Comparisons and Scientific Issues," *Journal of Geophysical Research*, Vol. 107, No. A12, 2002, pp. 1468–1483, doi: 10.1029/2002JA009430.
13. Vallado, D. A. and Crawford, P., "SGP4 Orbit Determination," *AIAA/AAS Astrodynamics Specialist Conference and Exhibit*, 2008, pp. 18–21.
14. Wang, R., Liu, J., and Zhang, Q., "Propagation errors analysis of TLE data," *Advances in Space Research*, Vol. 43, No. 7, 2009, pp. 1065–1069, doi: 10.1016/j.asr.2008.11.017.